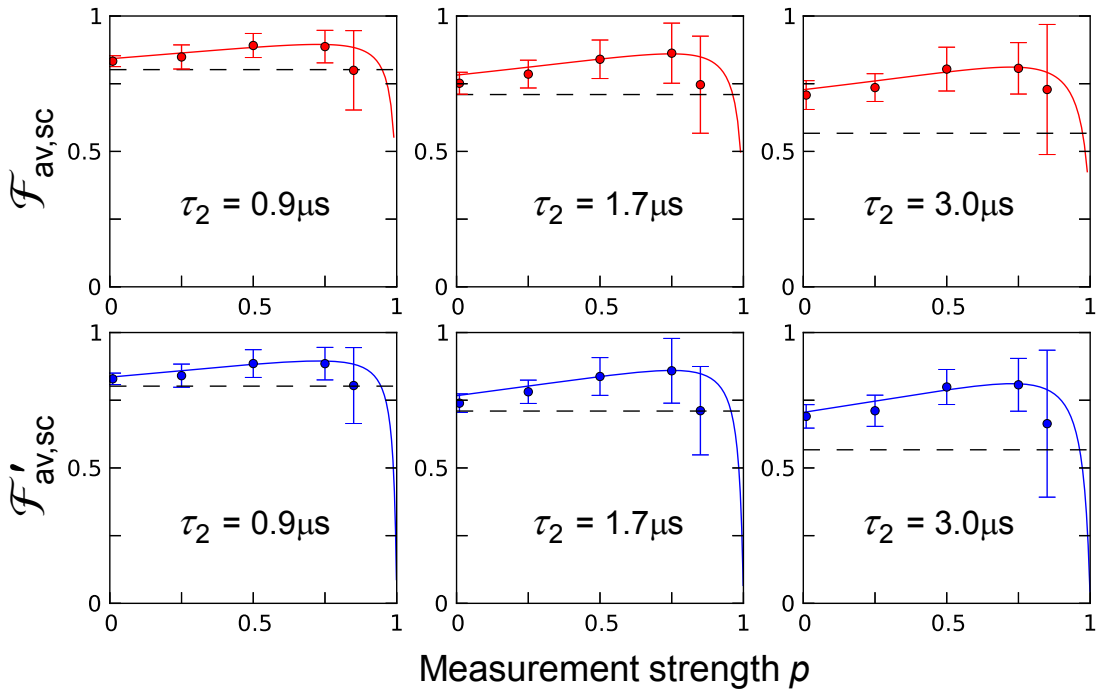

Supplementary Figure S1. **QEDR process fidelity characterized using different methods.** For the same experimental data as in Fig. 3a of the main text, here we show the QEDR process fidelities calculated via the averaged state fidelities $\mathcal{F}_{\mathrm{av}}$ and $\mathcal{F}'_{\mathrm{av}}$ defined in Eqs. (S29) and (S30). For easier comparison with Fig. 3a we show the scaled results $\mathcal{F}_{\mathrm{av,sc}} = (3\mathcal{F}_{\mathrm{av}} - 1)/2$ (top panels) and $\mathcal{F}'_{\mathrm{av,sc}} = (3\mathcal{F}'_{\mathrm{av}} - 1)/2$ (bottom panels). As in Fig. 3a, the quantum state is stored for the durations $\tau_2 = 0.9,\ 1.7$, and 3 μs in the memory resonator M_1, which has the energy relaxation time $T_1 = 2.5\,\mu$s. The measurement strength (swap probability) p is indicated on the horizontal axis, and the uncollapsing swap probability p_{u} is adjusted as described in the main text. Circles are the experimental results, while error bars represent statistical errors (standard deviation); lines are simulations. Horizontal dashed lines in each panel show the free-decay process fidelity. The statistical errors increase with increasing measurement strength p due to the decrease in sample size (fewer double-null outcomes). It is seen that all definitions of the QEDR process fidelity give similar results, and all of them show significant increase of the storage fidelity compared with the case of natural energy relaxation.

	freq. (GHz)	T_1 (ns)	T_2 (ns)	T_{SE} (ns)	coupling strength (MHz)
Q_1	6.01	580	140	500	34.7 ($\leftrightarrow B$)
Q_2	5.90	614	100	510	34.1 ($\leftrightarrow B$)
Q_3	5.81	580	150	430	33.3 ($\leftrightarrow B$)
B	6.24	3000	~5000	$*$	
M_1	7.55	2500	~5000	$*$	56.8 ($\leftrightarrow Q_1$)

Supplementary Table S1. **Operating characteristics for qubits Q_1, Q_2, Q_3, the bus resonator B, and the memory resonator M_1.** We show the $|g\rangle - |e\rangle$ splitting frequency for the qubits, the resonance frequency for the resonators, as well as each element's measured energy relaxation time T_1, Ramsey dephasing time T_2, and spin-echo dephasing time T_{SE}. Qubit lifetimes are at the listed frequencies, and resonator lifetimes are measured using photon swaps with a qubit; the coupling strengths are from vacuum Rabi oscillations. [27-29]

SUPPLEMENTARY NOTE 1
Sample fabrication

The qubits and resonators used in this experiment were all produced in a multi-layer lithographic process on single-crystal sapphire substrates. The qubits are phase qubits, each consisting of a 2 μm^2 Al/AlO_x/Al junction in parallel with a 1 pF Al/a-Si:H/Al shunt capacitor and a 720 pH loop inductance (design values). The resonators are single-layer aluminum coplanar waveguide resonators. We use interdigitated coupling capacitors between the qubits and the resonators. Standard performance parameters of individual elements are listed in Supplementary Table S1.

SUPPLEMENTARY NOTE 2
State evolution during the QRQ-based quantum error detection protocol

In this note we discuss the state evolution in the actual experimental protocol, based on the QRQ swaps. We include the dynamic phases in the analysis but for simplicity neglect imperfections as well as decoherence in the unitary operations, while including energy relaxation during the state storage in the memory resonator (step 2 in Fig. 1e of the main text).

Instead of using the master equation formalism for the density matrix to account for the energy relaxation, we work with wavefunctions and unravel the process into the jump (energy relaxation event) and no-jump scenarios (for more detail, see Refs. [21], [22], and Appendices of Ref. [34]). This is essentially the technique of Kraus operators, in which the zero-temperature energy relaxation ($|1\rangle \rightarrow |0\rangle$) during time τ of the memory resonator with energy relaxation time T_1 is represented by two Kraus operators: $A_{\rm jump} = \sqrt{1-\exp(-\tau/T_1)}\,|0\rangle\langle 1|$ and $A_{\rm no-jump} = |0\rangle\langle 0| + \exp(-\tau/2T_1)\,|1\rangle\langle 1|$. It is easy to check that the density matrix $A_{\rm jump}|\psi_{\rm i}\rangle\langle\psi_{\rm i}|A_{\rm jump}^{\dagger} + A_{\rm no-jump}|\psi_{\rm i}\rangle\langle\psi_{\rm i}|A_{\rm no-jump}^{\dagger}$ coincides with the density matrix obtained via the master equation, starting with an arbitrary initial state $|\psi_{\rm i}\rangle$. This technique of Kraus operators is convenient because of two reasons: First, it is easier to work with wavefunctions than with density matrices, and this gives more physical insight into the analyzed process. Second, the technique of Kraus operators is naturally compatible with the description of partial quantum measurements and/or projective measurements with post-selection.

Assuming no errors in the preparation of the target qubit Q_1, the initial state of the system prior to step 1 shown in Fig. 1e is [see Eq. (2) in the main text]

$$|\Psi_{\rm i}\rangle = \alpha|ggg\rangle|00\rangle + \beta|egg\rangle|00\rangle = (\alpha|g\rangle + \beta|e\rangle) \otimes |gg\rangle|00\rangle, \tag{S1}$$

where $|\alpha|^2 + |\beta|^2 = 1$ and the notation $|q_1\, q_2\, q_3\rangle\,|b\, m_1\rangle$ displays the quantum states of the qubits Q_1, Q_2, and Q_3, as well as the states of the bus B and memory M_1 resonators; the notation including the outer product sign $\otimes$ uses the same order for the system elements.

Step 1 of the procedure (Fig. 1e) is equivalent to the first partial measurement of the qubit Q_1 in Fig. 1a with strength p. This step consists of the QRQ swap Q_1–B–Q_2, followed by measurement of qubit Q_2. First, the partial swap between the qubit Q_1 and bus B with the swap probability p results in the state

$$|\Psi_{\rm 1a}\rangle = \alpha|ggg\rangle|00\rangle + \beta e^{i\theta_p}(\sqrt{1-p}\,|egg\rangle|00\rangle - ie^{i\tilde{\theta}_p}\sqrt{p}\,|ggg\rangle|10\rangle), \tag{S2}$$

where θ_p and $\tilde{\theta}_p$ are the dynamic phases accumulated when the frequency of qubit Q_1 is tuned into and out of resonance with the resonator B [each term in Eq. (S2) assumes a separate rotating frame]. The factor $-i$ in the last term comes from the ideal qubit-resonator evolution described by the standard Hamiltonian. After this partial swap, the resonator B is no longer in the ground state. The second part of the QRQ swap fully transfers the

excitation from B into Q_2, resulting in the state

$$|\Psi_{1b}\rangle = \alpha|ggg\rangle|00\rangle + \beta e^{i\theta_p}(\sqrt{1-p}\,|egg\rangle|00\rangle - \sqrt{p}\,e^{i\theta_{pa}}|geg\rangle|00\rangle), \tag{S3}$$

where the phase θ_{pa} combines $\tilde{\theta}_p$ and the dynamic phase accumulated during the full swap. The minus sign in the last term is due to the additional factor $-i$, appearing when the excitation in the resonator B swaps to Q_2 (this is why the full swap is termed an iSWAP).

After the QRQ swap Q_1–B–Q_2, the qubit Q_2 is measured projectively (strongly) and only the outcome $|g\rangle$ is selected. Phase qubits are measured [28] by lowering the tunnel barrier between the right and left potential wells shown in the bottom panel of Fig. 1a, with a high likelihood of tunneling to the right well if the qubit is in the excited state $|e\rangle$, while there is a very small tunneling probability if the qubit is in its ground state $|g\rangle$. When a qubit that is initially in a superposition of $|g\rangle$ and $|e\rangle$ tunnels to the right well, the subsequent rapid energy decay in the right well destroys any coherence between $|g\rangle$ and $|e\rangle$ states. The barrier is lowered only for a few nanoseconds, and the quantum state projection occurs during this time. Actual readout of the measurement result takes place many microseconds later, using a SQUID flux measurement.

In the case of the measurement result $|g\rangle$ (no tunneling for qubit Q_2), the system state (S3) collapses to the state

$$|\Psi_{1c}\rangle = \alpha|ggg\rangle|00\rangle + \beta e^{i\theta_p}\sqrt{1-p}\,|egg\rangle|00\rangle. \tag{S4}$$

Notice that while the state (S3) is normalized, $\langle\Psi_{1b}|\Psi_{1b}\rangle = 1$, the post-selected state (S4) is not normalized, so that $\langle\Psi_{1c}|\Psi_{1c}\rangle$ is the probability of the $|g\rangle$ outcome, while the normalized state would be $|\Psi_{1c}\rangle/\sqrt{\langle\Psi_{1c}|\Psi_{1c}\rangle}$. We prefer here to use unnormalized states as in Eq. (S4) because these are linearly related to the initial state, in contrast to the normalized states. The state (S4) can be written as $|\Psi_{1c}\rangle = (\alpha|g\rangle + \beta e^{i\theta_p}\sqrt{1-p}\,|e\rangle)\,|gg\rangle|00\rangle$, so at the end of this step we essentially have a one-qubit state in Q_1, even though other elements of the system are entangled with Q_1 during the evolution of this step.

Step 2 of the protocol (Fig. 1e) involves storing Q_1's state in the memory resonator M_1 for a relatively long time τ_2, which corresponds to the delay τ in the protocol in Fig. 1a in the main text. We first perform an iSWAP between Q_1 and M_1, resulting in the state

$$|\Psi_{2a}\rangle = \alpha|ggg\rangle|00\rangle - i\beta e^{i\theta_p}e^{i\tilde{\theta}_s}\sqrt{1-p}\,|ggg\rangle|01\rangle, \tag{S5}$$

where $\tilde{\theta}_\mathrm{s}$ is the dynamic phase accumulated when tuning Q_1 into the resonance with M_1. With Q_1 now in its ground state, we detune Q_1 from M_1 to its idle frequency, and wait a time τ_2. During this time the state in the resonator M_1 decays in energy at the rate $\Gamma = 1/T_1$, where $T_1 = 2.5\,\mu$s is the energy relaxation time of M_1, so that the overall decay factor is $\kappa_2 = e^{-\Gamma\tau_2}$ (pure dephasing is negligible).

The decay in M_1 can be treated by considering two scenarios [22]: either the state of M_1 jumps to $|0\rangle$ during the storage time τ_2 or there is no jump (see the brief discussion above). In the jump scenario the resulting unnormalized state is

$$|\Psi_{2\mathrm{b}}^{\mathrm{j}}\rangle = \beta\sqrt{1-p}\,\sqrt{1-e^{-\Gamma\tau_2}}\,|ggg\rangle|00\rangle, \tag{S6}$$

where the overall phase is not important. Note that the first term in Eq. (S5) does not give a contribution to $|\Psi_{2\mathrm{b}}^{\mathrm{j}}\rangle$. Physically, this is because the jump cannot occur when M_1 is in the ground state $|0\rangle$. Mathematically, this is because application of the corresponding Kraus operator A_{jump} to the first term of Eq. (S5) gives zero.

We will return to the jump scenario later, focusing first on the no-jump scenario, which produces the unnormalized state

$$|\Psi_{2\mathrm{b}}^{\mathrm{nj}}\rangle = \alpha|ggg\rangle|00\rangle - i\beta e^{i\theta_p}e^{i\tilde{\theta}_\mathrm{s}}\sqrt{1-p}\,e^{-\Gamma\tau_2/2}|ggg\rangle|01\rangle. \tag{S7}$$

After the storage time τ_2 we swap the state in M_1 back to Q_1, so that at the end of step 2 the no-jump state becomes

$$|\Psi_{2\mathrm{c}}^{\mathrm{nj}}\rangle = \alpha|ggg\rangle|00\rangle + \beta e^{i(\theta_p+\theta_\mathrm{s})}\sqrt{1-p}\,e^{-\Gamma\tau_2/2}|egg\rangle|00\rangle, \tag{S8}$$

where the phase θ_s includes $\tilde{\theta}_\mathrm{s}$ [see Eq. (S5)], the similar dynamic phase accumulated during the swap back to Q_1, the π-shift due to the factor $(-i)^2$, and the phase $2\pi\Delta f\tau_2$ accumulated due to the frequency difference Δf between the resonator M_1 and the qubit Q_1 at its idle frequency. After the step is completed, we again have essentially a one-qubit state.

Step 3 of the protocol consists of a π_x rotation, the second QRQ swap Q_1–B–Q_3 with strength p_u, and the projective measurement of Q_3 (this step is analogous to the second partial measurement in Fig. 1a). The π_x rotation applied to Q_1 exchanges the amplitudes of its $|g\rangle$ and $|e\rangle$ states in Eq. (S8):

$$|\Psi_{3\mathrm{a}}^{\mathrm{nj}}\rangle = \alpha|egg\rangle|00\rangle + \beta e^{i(\theta_p+\theta_\mathrm{s})}\sqrt{1-p}\,e^{-\Gamma\tau_2/2}|ggg\rangle|00\rangle. \tag{S9}$$

The partial swap between Q_1 and B then yields the state

$$|\Psi_{3b}^{nj}\rangle = \alpha e^{i\theta_u}(\sqrt{1-p_u}\,|egg\rangle|00\rangle - ie^{i\tilde{\theta}_u}\sqrt{p_u}\,|ggg\rangle|10\rangle) + \beta e^{i(\theta_p+\theta_s)}\sqrt{1-p}\,e^{-\Gamma\tau_2/2}|ggg\rangle|00\rangle, \tag{S10}$$

where θ_u and $\tilde{\theta}_u$ are the dynamic phases accumulated during this partial swap. Next, the QRQ swap is completed with a full iSWAP between B and Q_3, yielding the state

$$\begin{aligned}|\Psi_{3c}^{nj}\rangle = [&(e^{i\theta_u}\alpha\sqrt{1-p_u}\,|egg\rangle + e^{i(\theta_p+\theta_s)}\beta\sqrt{1-p}\,e^{-\Gamma\tau_2/2}|ggg\rangle)\\ &-e^{i(\theta_u+\theta_{ua})}\alpha\sqrt{p_u}\,|gge\rangle] \otimes |00\rangle,\end{aligned} \tag{S11}$$

where θ_{ua} combines $\tilde{\theta}_u$ and the dynamic phase accumulated during the last iSWAP. Finally, the measurement of Q_3 and the selection of the result $|g\rangle$ (thus corresponding to an overall double-null outcome) produces the no-jump state

$$|\Psi_f^{nj}\rangle = (\alpha\sqrt{1-p_u}\,|e\rangle + e^{i(\theta_p+\theta_s-\theta_u)}\beta\sqrt{1-p}\,e^{-\Gamma\tau_2/2}|g\rangle) \otimes |gg\rangle|00\rangle, \tag{S12}$$

where we ignore the unimportant overall phase.

Equation (S12) coincides with Eq. (3) of the main text, if we neglect the dynamic phase $\theta_p+\theta_s-\theta_u$. This phase does not depend on the initial state, but in general depends on p, p_u, and τ_2. To restore the initial qubit state (up to a π_x rotation), this phase can be corrected by an additional single-qubit phase gate (rotation about the z axis of the Bloch sphere). In the experiment we typically did not perform this correction, and instead compensated for this phase numerically in the quantum process tomography analysis. However, we have checked explicitly that for the initial states $|g\rangle - i\,|e\rangle$ and $|g\rangle + |e\rangle$ (using the same QEDR protocol parameters), the measured output states differ by a phase of $\pi/2$, as expected.

Note that we completely omit step 2 when testing the protocol with no storage in M_1, i.e. with $\tau_2 = 0$ (see Fig. 2 of the main text). In this case there is no dynamic phase θ_s in Eq. (S12), we have no delay-based decay so that $e^{-\Gamma\tau_2/2} = 1$, and also the dynamic phases θ_p and θ_u cancel each other because $p_u = p$ and therefore $\theta_u = \theta_p$. In reality there is still a small amount of energy decay occurring in steps 1 and 3. We take this into account in the numerical simulations as described in Supplementary Note 3.

Now let us return to the scenario when the energy relaxation event (the jump) occurs during step 2, producing the state $|\Psi_{2b}^{j}\rangle$ given by Eq. (S6). After performing the swap between the memory resonator and Q_1, this state remains the same, $|\Psi_{2c}^{j}\rangle = |\Psi_{2b}^{j}\rangle$, because

all elements are in their ground states. In step 3 of the protocol, following the π_x pulse, the state becomes

$$|\Psi^{j}_{3a}\rangle = \beta\sqrt{1-p}\,\sqrt{1-e^{-\Gamma\tau_2}}\,|egg\rangle|00\rangle, \tag{S13}$$

and following the partial swap between Q_1 and B this state evolves into

$$|\Psi^{j}_{3b}\rangle = \beta\sqrt{1-p}\,\sqrt{1-e^{-\Gamma\tau_2}}\,(\sqrt{1-p_u}\,|egg\rangle|00\rangle - ie^{i\tilde{\theta}_u}\sqrt{p_u}\,|ggg\rangle|10\rangle) \tag{S14}$$

(the overall phase θ_u is now unimportant), and after the full iSWAP between B and Q_3 it becomes

$$|\Psi^{j}_{3c}\rangle = \beta\sqrt{1-p}\,\sqrt{1-e^{-\Gamma\tau_2}}\,(\sqrt{1-p_u}\,|egg\rangle - e^{i\theta_{ua}}\sqrt{p_u}\,|gge\rangle)\otimes|00\rangle. \tag{S15}$$

After the measurement of Q_3 and selection of the null result $|g\rangle$, the final state in the jump scenario is

$$|\Psi^{j}_{f}\rangle = \beta\sqrt{1-p}\,\sqrt{1-e^{-\Gamma\tau_2}}\,\sqrt{1-p_u}\,|e\rangle\otimes|gg\rangle|00\rangle, \tag{S16}$$

so that the qubit Q_1 is now in the $|e\rangle$ state.

The squared norm of the no-jump final state $|\Psi^{nj}_{f}\rangle$ in Eq. (S12) is the probability of the no-jump scenario (which includes the double-null outcome selection),

$$P^{nj}_{f} \equiv \langle\Psi^{nj}_{f}|\Psi^{nj}_{f}\rangle = |\alpha|^2(1-p_u) + |\beta|^2(1-p)e^{-\Gamma\tau_2}. \tag{S17}$$

Notice that this probability becomes $P^{nj}_{f} = (1-p)e^{-\Gamma\tau_2}$ if we choose $1-p_u = (1-p)e^{-\Gamma\tau_2}$. The squared norm of the state $|\Psi^{j}_{f}\rangle$ in Eq. (S16) is the probability of the jump scenario,

$$P^{j}_{f} \equiv \langle\Psi^{j}_{f}|\Psi^{j}_{f}\rangle = |\beta|^2(1-p)(1-p_u)(1-e^{-\Gamma\tau_2}). \tag{S18}$$

This probability is given by $P^{j}_{f} = |\beta|^2(1-p)^2e^{-\Gamma\tau_2}(1-e^{-\Gamma\tau_2})$ if we choose $1-p_u = (1-p)e^{-\Gamma\tau_2}$. The probabilities P^{nj}_{f} and P^{j}_{f} cover all possible double-null outcomes in this model, so their sum

$$P_{DN} = P^{nj}_{f} + P^{j}_{f} \tag{S19}$$

is the probability of the double-null outcome.

Combining the two scenarios, the normalized density matrix of the system after the selection of the double-null outcome is

$$\rho_f = \frac{|\Psi^{nj}_{f}\rangle\langle\Psi^{nj}_{f}| + |\Psi^{j}_{f}\rangle\langle\Psi^{j}_{f}|}{P_{DN}}. \tag{S20}$$

In this double-null outcome, note that the target qubit Q_1 is now unentangled with the other elements, which are all in their ground states. Comparing the resulting state of the qubit Q_1 with the corresponding final state in the single-qubit protocol based on partial tunneling [see Fig. 1a and Eq. (1) in the main text], we see only two differences: the non-zero dynamic phase $\theta_p+\theta_\mathrm{s}-\theta_\mathrm{u}$ in Eq. (S12), and the exchange of the amplitudes of the states $|g\rangle$ and $|e\rangle$ due to the absence of the final π_x pulse. Therefore, our experimental protocol shown in Fig. 1e essentially realizes the un-collapsing protocol shown in Fig. 1a, but with much better experimental fidelity.

SUPPLEMENTARY NOTE 3
Numerical simulations

For numerical simulations we follow the theory of Ref. [22] and describe decoherence by the energy relaxation factors κ_1, κ_2, and κ_3 (each factor for the corresponding step of the protocol shown in Fig. 1e) and by the factor κ_φ, which accounts for pure dephasing during the whole procedure. The primary decay factor is $\kappa_2 \approx \exp(-\tau_2/T_1)$, where $\tau_2 = \tau$ is the storage time and $T_1 = 2.5\,\mu$s is the energy relaxation time of the memory resonator. Similarly, κ_1 describes energy relaxation before the first partial measurement and κ_3 describes energy relaxation in between the π_x pulse and the second partial measurement. Therefore $\kappa_1 = \exp(-\tilde{\tau}_1/T_1^{(1)})$ and $\kappa_3 = \exp(-\tilde{\tau}_3/T_1^{(3)})$, where $\tilde{\tau}_1$ is the effective duration of step 1 in Fig. 1e before the quantum information is partially swaped into the bus resonator, $\tilde{\tau}_3$ is the effective duration of step 3 between the π_x pulse and partial swap into the bus resonator, and $T_1^{(1)}$ and $T_1^{(3)}$ are the effective energy relaxation times for these steps (mostly determined by the phase qubit Q_1). We estimate that $\kappa_1 \approx \kappa_3 \approx 0.985$, consistent with the energy relaxation time $T_1 \simeq 0.6\ \mu$s of the phase qubit Q_1 (see Supplementary Table S1) and the time ~ 10 ns, which the quantum state spends in the phase qubit before the first partial swap (in step 1) and between the π_x pulse and the second partial swap (in step 3).

The overall pure dephasing factor is $\kappa_\varphi = \exp[-\tau_1/T_\varphi^{(1)} - \tau_2/T_\varphi^{(2)} - \tau_3/T_\varphi^{(3)}]$, where $T_\varphi^{(i)}$ is the effective pure dephasing time during ith step ($1/T_\varphi = 1/T_2 - 1/2T_1$). In simulations we used the value $\kappa_\varphi = 0.95$, which fits well with the experimental results and is consistent with the qubit parameters in Supplementary Table S1. Notice that $T_\varphi^{(2)}$ is very long since during step 2, the quantum state is stored in the memory resonator, and therefore κ_φ does not depend on τ_2. Also notice that because of the π_x pulse in the procedure (see Fig. 1e),

pure dephasing is reduced, essentially due to a spin-echo effect. In the theory we neglect imperfections of the unitary gates and the qubit decoherence after the second partial swap; we also do not accurately consider decoherence processes in the actual multi-component device, essentially reducing it to the single-qubit model of Ref. [22]. In a practical sense, however, these additional imperfections are somewhat accounted for by small adjustments of the parameters κ_1, κ_3, and κ_φ. We have checked numerically that slight variations of the parameters κ_1, κ_3, and κ_φ do not affect the simulation results significantly; κ_3 is the most important parameter, and varying its value in the experimentally-expected range of 0.985 ± 0.005 gives good agreement with the data shown in Fig. 3a of the main text.

In the experiment we do not perform the final π_x rotation to save time, so in the final state the amplitudes of the states $|g\rangle$ and $|e\rangle$ are exchanged in comparison with the initial state $|\psi_\mathrm{i}\rangle = \alpha\,|g\rangle + \beta\,|e\rangle$ in Q_1 (here and below we use a lowercase $|\psi\rangle$ to represent the state of Q_1, in contrast to $|\Psi\rangle$ which represents the state of the complete system of 3 qubits and 2 resonators). Following the approach of Ref. [22], neglecting the dynamic phases, and for the moment neglecting pure dephasing, we can represent the state of the qubit Q_1 after the double-null outcome selection as an incoherent mixture of the three states $|g\rangle$, $|e\rangle$, and

$$|\psi_\mathrm{f}^\mathrm{nj}\rangle = \beta\sqrt{\kappa_1\kappa_2(1-p)}\,|g\rangle + \alpha\sqrt{\kappa_3(1-p_\mathrm{u})}\,|e\rangle\,. \tag{S21}$$

The unnormalized state $|\psi_\mathrm{f}^\mathrm{nj}\rangle$ occurs in the no-jump scenario during steps 1, 2, and 3. The squared norm of this wavefunction is the probability of the no-jump scenario,

$$P_\mathrm{f}^\mathrm{nj} = \langle\psi_\mathrm{f}^\mathrm{nj}|\psi_\mathrm{f}^\mathrm{nj}\rangle = |\alpha|^2\,\kappa_3(1-p_\mathrm{u}) + |\beta|^2\,\kappa_1\kappa_2(1-p), \tag{S22}$$

which includes the probability of the double-null outcome selection.

The final state $|g\rangle$ is realized if there was a jump to $|g\rangle$ after the π_x pulse in step 3 and there was zero or one jump during steps 1 and 2. This occurs with the probability

$$P_\mathrm{f}^{|g\rangle} = (1-\kappa_3)\,|\alpha|^2 + (1-\kappa_3)\,|\beta|^2\,[(1-\kappa_1) + \kappa_1(1-p)(1-\kappa_2)], \tag{S23}$$

which can be easily understood in the classical way (for a qubit starting either in the state $|g\rangle$ or $|e\rangle$). The final state $|e\rangle$ is realized if there was a jump either during step 1 or 2 and no jump during step 3; this occurs with probability

$$P_\mathrm{f}^{|e\rangle} = |\beta|^2\,[(1-\kappa_1) + \kappa_1(1-p)(1-\kappa_2)]\kappa_3(1-p_\mathrm{u}). \tag{S24}$$

Combining these three scenarios, we obtain the normalized density matrix of the qubit final state:

$$\rho_{\rm f} = \frac{|\psi_{\rm f}^{\rm nj}\rangle\langle\psi_{\rm f}^{\rm nj}| + P_{\rm f}^{|g\rangle}|g\rangle\langle g| + P_{\rm f}^{|e\rangle}|e\rangle\langle e|}{P_{\rm DN}}, \tag{S25}$$

where

$$P_{\rm DN} = P_{\rm f}^{\rm nj} + P_f^{|g\rangle} + P_f^{|e\rangle} \tag{S26}$$

is the probability of the double-null outcome. Notice that there is no factor $P_{\rm f}^{\rm nj}$ in the numerator of Eq. (S25) because it was included in the definition of the unnormalized state $|\psi_{\rm f}^{\rm nj}\rangle$ in Eq. (S21). The unnormalized final density matrix $P_{\rm DN}\rho_{\rm f}$ [the numerator in Eq. (S25)] is linearly related to the initial density matrix $\rho_{\rm i} = |\psi_{\rm i}\rangle\langle\psi_{\rm i}|$, so the linear map used in the analysis of the quantum process tomography is $\rho_{\rm i} \to P_{\rm DN}\rho_{\rm f}$.

Pure dephasing (described by κ_φ) does not affect the probabilities and does not affect the final states $|g\rangle$ and $|e\rangle$. The only effect of pure dephasing is that the off-diagonal matrix elements of $|\psi_{\rm f}^{\rm nj}\rangle\langle\psi_{\rm f}^{\rm nj}|$ are multiplied by κ_φ. Including dephasing, the system's density matrix after the selection of the double-null outcome is given by

$$\rho_{\rm f} = \frac{1}{P_{\rm DN}} \begin{bmatrix} \kappa_1\kappa_2(1-p)|\beta|^2 + P_{\rm f}^{|g\rangle} & \kappa_\varphi\sqrt{\kappa_1\kappa_2\kappa_3(1-p)(1-p_{\rm u})}\beta^*\alpha \\ \kappa_\varphi\sqrt{\kappa_1\kappa_2\kappa_3(1-p)(1-p_{\rm u})}\beta\alpha^* & \kappa_3(1-p_{\rm u})|\alpha|^2 + P_{\rm f}^{|e\rangle} \end{bmatrix}. \tag{S27}$$

Using Eq. (S27), we can calculate the process matrix χ and the process fidelity.

The dynamic phases appearing in the actual experimental procedure affect only the relative phase between the two terms in Eq. (S21). Therefore, the dynamic phases can be taken into account by using a single parameter: the phase shift of the off-diagonal element of the final density matrix. This dynamic phase shift depends on the parameters of the experimental protocol, including the strength p and $p_{\rm u}$ of the two partial measurements (partial swaps) and the storage duration τ_2.

Numerical simulations in this paper are based on Eq. (S27), so they are relatively simple and mostly involve evaluation of (rather lengthy) formulas. As the efficiency of the QEDR protocol depends on the value of $p_{\rm u}$ once p is fixed, we performed an error analysis of the process fidelity $\mathcal{F}$ based on the uncertainty in $p_{\rm u}$. Once p is chosen, the optimal $p_{\rm u}$ value depends on the intrinsic decay rate Γ of the resonator and the decay time τ_2, which can be precisely determined in the experiment. We then choose the QRQ swap time that

corresponds to the optimal $p_{\rm u}$ value. Errors in the QRQ swap time thus introduce errors through the effective variation of $p_{\rm u}$; we have found experimentally that the uncertainty in $p_{\rm u}$ is about 0.02. To test the sensitivity of $\mathcal{F}$ to errors in $p_{\rm u}$, we performed numerical simulations using Eq. (S27). We find that the uncertainty in $\mathcal{F}$ due to the uncertainty in $p_{\rm u}$ is very small for all the data shown in Fig. 3a in the main text, corresponding to less than 10% of the error bars shown in the figure. This suggests that the process fidelity errors come mainly from statistical errors due to the small sample size rather than uncertainty in $p_{\rm u}$.

SUPPLEMENTARY NOTE 4
Analysis of the QEDR process fidelity

In the main text we use the definition [31]

$$\mathcal{F} = \frac{\mathrm{Tr}(\chi^{\rm ideal}\chi)}{\mathrm{Tr}(\chi)}, \tag{S28}$$

for the process fidelity of a non-trace-preserving quantum operation. This definition implies that $\chi/\,\mathrm{Tr}(\chi)$ is the effective process matrix (which is shown e.g. in Fig. 2a of the main text). Notice that $\chi/\,\mathrm{Tr}(\chi)$ does not correspond to any physical trace-preserving process; however, this is a positive Hermitian matrix with unit trace, and therefore $0 \le \mathcal{F} \le 1$ when $\chi^{\rm ideal}$ corresponds to a unitary operation. The perfect fidelity, $\mathcal{F} = 1$, requires $\chi = P_{\rm s}\chi^{\rm ideal}$ with $P_{\rm s} \le 1$ being the selection probability (in this case $P_{\rm s}$ should not depend on the initial state). This justifies the definition (S28).

However, Eq. (S28) is not the only possible definition for the fidelity of a non-trace-preserving quantum process. For example, another natural definition [22] is the averaged state fidelity,

$$\mathcal{F}_{\rm av} = \frac{\int \mathrm{Tr}(\rho_{\rm f}\rho_{\rm f}^{\rm ideal})\, d|\psi_{\rm i}\rangle}{\int d|\psi_{\rm i}\rangle}, \tag{S29}$$

where $\rho_{\rm f}^{\rm ideal} = U|\psi_{\rm i}\rangle\langle\psi_{\rm i}|U^\dagger$, U is the desired unitary operation, $\rho_{\rm f}$ is the actual normalized density matrix, and the integration is over all pure initial states $|\psi_{\rm i}\rangle$ with uniform weight (using the Haar measure); in the one-qubit case this is the uniform averaging over the Bloch sphere. Another natural definition is the averaged state fidelity, which is averaged with a weight proportional to the selection probability $P_{\rm s}$ (denoted $P_{\rm DN}$ in the main text),

$$\mathcal{F}'_{\rm av} = \frac{\int \mathrm{Tr}(\rho_{\rm f}\rho_{\rm f}^{\rm ideal}) P_{\rm s}(|\psi_{\rm i}\rangle)\, d|\psi_{\rm i}\rangle}{\int P_{\rm s}(|\psi_{\rm i}\rangle)\, d|\psi_{\rm i}\rangle}. \tag{S30}$$

Notice that both $\mathcal{F}_{\rm av}$ and $\mathcal{F}'_{\rm av}$ can be easily calculated when the process matrix χ is known.

For a trace-preserving quantum operation $\mathcal{F}'_{\rm av} = \mathcal{F}_{\rm av}$ because $P_{\rm s} = 1$, and there is a direct relation [33] $\mathrm{Tr}(\chi^{\rm ideal}\chi) = [(d+1)\mathcal{F}_{\rm av} - 1]/d$, where d is the dimension of the Hilbert space ($d = 2$ in our one-qubit case). It is possible to show that in the general non-trace-preserving case the same relation remains valid between $\mathcal{F}$ defined by Eq. (S28) and $\mathcal{F}'_{\rm av}$ defined by Eq. (S30),

$$\mathcal{F} = \frac{(d+1)\,\mathcal{F}'_{\rm av} - 1}{d}. \tag{S31}$$

Notice that the denominator $\mathrm{Tr}(\chi)$ in Eq. (S28) is equal to the averaged selection probability,

$$\mathrm{Tr}(\chi) = \frac{\int P_{\rm s}(|\psi_{\rm i}\rangle)\, d|\psi_{\rm i}\rangle}{\int d|\psi_{\rm i}\rangle}. \tag{S32}$$

We have numerically calculated the process fidelity in our un-collapsing QEDR experiment using all three definitions (S28)–(S30). For easier comparison with the results for $\mathcal{F}$ shown in Fig. 3a of the main text, in Fig. S1 we scale $\mathcal{F}_{\rm av}$ and $\mathcal{F}'_{\rm av}$ as in Eq. (S31): $\mathcal{F}_{\rm av,sc} = (3\mathcal{F}_{\rm av} - 1)/2$, $\mathcal{F}'_{\rm av,sc} = (3\mathcal{F}'_{\rm av} - 1)/2$. Notice that for the experimental results $\mathcal{F}'_{\rm av,sc}$ and $\mathcal{F}$ are not exactly equal to each other [in spite of Eq. (S31)] because slightly different algorithms were used in the numerical processing of the over-complete experimental data set. Comparing Supplementary Figure S1 with Fig. 3a, we see that the experimental results using the three fidelity definitions are close to each other, and all of them show significant increase of the fidelity due to the un-collapsing-based QEDR procedure.

SUPPLEMENTARY NOTE 5
QEDR versus Quantum Error Correction

We now briefly discuss the relation between the QEDR procedure and quantum error correction (QEC). The main difference is that QEDR is a selective process (which selects only certain measurement results) and therefore is necessarily probabilistic, although with potentially high fidelity in the selected outcomes. By contrast, QEC can in principle achieve 100% probability, even if its fidelity is low. Since QEDR works probabilistically, there are clearly serious problems with scaling, similar to those with proposals for quantum computers based on linear optics [35]. We therefore do not believe that QEDR is practical for large-scale quantum information processing.

It would of course be very interesting to implement quantum error correction using our circuit, but we have been unable to do this, primarily due to inadequate gate fidelities, limited in part by the T_2 of our qubits. This can be seen by the fact that a typical two qubit CNOT gate takes ~ 50 ns in our device. As this is already about 30% of the T_2 time of 150 ns, dephasing significantly impacts our CNOT fidelity. Building a code that could correct amplitude damping (dissipation) errors in one qubit will, in one scheme, require 4 physical qubits and a number of gate operations including the CNOT [18]; performing this kind of error correction remains a challenge for experimentalists.

An alternative recent proposal uses a circuit QED structure to encode/decode the qubit state in order to correct for photon dissipation errors [19]. This proposal uses fewer qubits than that of Ref. [18], but still requires a number of complex gates, and has not yet been realized experimentally. Interestingly, a numerical simulation for this proposal suggests that an improvement of only a factor of two in the resonator lifetime can be achieved, even if the QEC gate execution is almost perfect. We note that this is smaller than the factor of three effective improvement demonstrated in our QEDR experiment.

As QEC of energy relaxation errors in superconducting qubits is presently not possible, QEDR provides a good intermediate method, here demonstrating a factor of three improvement in the effective lifetime of a quantum state. Furthermore, even if QEC becomes a viable approach in the future, QEDR may still be useful in medium-scale quantum information processing.

Note that the detection of quantum errors and selection of no-error realizations is not as trivial as in the classical case. For example, one may think that to do the QEDR for the qubit energy relaxation it is sufficient to monitor the emission of a photon (or phonon) and then select only the realizations without the emission event. However, besides the technical problems with practical implementation of such gedankenexperiment, it would not work as QEDR even theoretically, because observation of no emission changes the qubit state, $|\psi_{\rm i}\rangle \rightarrow A_{\rm no-jump}|\psi_{\rm i}\rangle$ (see the second paragraph in Supplementary Note 2).

Besides its potential practical use in the future, QEDR has value as it provides a stepping stone towards the more-practical QEC, as it essentially demonstrates the same "magic" of a quantum algorithm that is able to deal with the continuous evolution of a quantum state (or density matrix) due to decoherence, by essentially converting this continuous change into discrete jump events (errors). Our particular implementation of QEDR, based on the

reversal of a quantum measurement (which we note is often thought to be a fundamentally *irreversible* process), demonstrates non-trivial physics and shows that quite counterintuitive effects can be practically useful in quantum information processing.

SUPPLEMENTARY REFERENCES

[33] Nielsen, M. A. A simple formula for the average gate fidelity of a quantum dynamical operation. *Phys. Lett. A* **303**, 249 (2002).

[34] Korotkov, A. N. Error matrix in quantum process tomography. E-print arXiv:1309.6405.

[35] Knill E., Laflamme R., and Milburn, G. J. A scheme for efficient quantum computation with linear optics. *Nature* **409**, 46 (2001).